Quantitative geometry of the Rayleigh wave oscillation ellipse by surface acoustic wave scanning tunneling microscopy

P. U. Voigt and R. Koch[a)]
Paul-Drude-Institut für Festkörperelektronik, Hausvogteiplatz 5-7, D-10117 Berlin, Germany

(Received 14 August 2002; accepted 20 September 2002)

In recent studies it has been demonstrated that the scanning tunneling microscope (STM) after sophisticated modification is a powerful technique to investigate surface acoustic waves (SAWs) with high spatial resolution. Here we apply our ultrahigh vacuum (UHV) SAW–STM to investigate the surface motion induced by a Rayleigh wave on $LiNbO_3$. After establishing the theoretical basis for evaluating SAW–STM images recorded as usual in the constant–current scanning mode we apply the method to quantitatively determine the complete geometry of the atomic oscillation ellipse given by its eccentricity and the amplitude of the transverse displacement. The obtained eccentricity parameter is 36° being in good agreement with the theoretical value of 35.1°. Our investigations show that the dynamic range of our UHV–SAW–STM comprises at least 3 orders of magnitude down to SAW amplitudes as small as 0.001 Å and, furthermore, that the spatial resolution for acoustic measurements lies in the lower nanometer range. © *2002 American Institute of Physics*. [DOI: 10.1063/1.1520734]

I. INTRODUCTION

Surface acoustic waves (SAWs) are solutions of the wave equation of solid media with displacements decreasing with depth. Their existence was first predicted by Lord Rayleigh[1] in 1885 and in the following years SAWs were found to play a fundamental role in earthquakes.[2] The low propagation velocity of SAWs, which is 5 orders of magnitude smaller compared with electromagnetic waves, gives rise to a variety of SAW devices for signal processing. The present scientific interest in SAWs is not only justified by the wide-spread use of SAW devices especially in telecommunication systems. SAWs are also the topic of current basic research e.g., their role in the transport of spins[3] and carriers.[4]

In the recent years a variety of methods probing acoustic fields were developed. Optical methods utilize diffraction,[5] interference,[5] beam deflection,[6] and the influence of SAW-induced strain on optical reflectivity. Since the lateral resolution is limited by the wavelength of the chosen light, optical methods are not suited for mapping GHz range SAWs with wavelengths below the optical diffraction limit or studying the interaction of SAWs with nanometer-sized quantum objects. To overcome the optical resolution limit various scanning probe methods have been adapted for mapping of submicron acoustic wave fields. In scanning acoustic force microscopy—developed by Rohrbeck and Chilla[7]—the nonlinear force-to-distance dependence is employed to down-convert the high-frequency oscillation to the frequency range of an atomic force microscope (AFM), which enables detection of SAW amplitude and phase with nanometer resolution. As shown by Kolosov and Yamanka the normal component of the SAW amplitude gives also rise to a static deflection of the AFM cantilever,[8] which can be utilized to even discriminate subsurface features with different elastic properties.[9] By means of amplitude-modulated SAWs Strozewski *et al.*[10] demonstrated that also the scanning tunneling microscope (STM)—despite of its completely different frequency and length scales—is capable of probing SAWs. Chilla *et al.*[11,12] succeeded to down-convert the high frequency component in the tunneling current due to the SAW-induced surface oscillation ($\sim 10\,\mathrm{MHz} \rightarrow \sim \mathrm{GHz}$) to the kHz range, where it can be amplified by a conventional lock-in technique. The resulting SAW–STM signal exhibits the same phase and amplitude as the tunneling distance modulation (see Sec. II), thus offering the challenging opportunity to take advantage of the lateral resolution of the STM for nanoscale investigations of surface acoustic wave fields.

The Rayleigh wave, being the only surface wave mode in isotropic media, is the most prominent type of SAW. In crystals so-called Rayleigh-type waves exist in high symmetry directions which display the same characteristics as pure Rayleigh waves: Each surface element travels along an elliptic trajectory, called the oscillation ellipse, described by longitudinal and transverse displacements $u^{(1)}$ and $u^{(3)}$, respectively,

$$u^{(1)} = u_1 \cos(\omega_{\mathrm{SAW}} t - k_{\mathrm{SAW}} x_1), \tag{1}$$

$$u^{(3)} = u_3 \cos(\omega_{\mathrm{SAW}} t - k_{\mathrm{SAW}} x_1 - \pi/2). \tag{2}$$

Here u_1 and u_3 are the displacement amplitudes, and ω_{SAW} and k_{SAW} are angular frequency and wave vector of the SAW, respectively. Since the ratio u_1/u_3 is determined by the elastic constants, in principle, information about the local elastic properties can be gained from spatially resolved measurements of u_1/u_3. Unfortunately common experimental techniques are inadequate for determining u_1/u_3 because they do not measure both displacement amplitudes separately: Heil *et al.*[13] used a conventional STM to deduce the longitudinal

a)Author to whom correspondence should be addressed; electronic mail: koch@pdi-berlin.de

displacement of ultrasonic waves from topographical images. The transverse displacement, on the other hand, is accessible to interferometrical methods[5] and to x-ray diffraction mapping of SAWs.[14] The SAW–STM technique presented here closes the gap in the variety of methods introduced so far: the SAW–STM is not only capable of achieving atomic resolution in imaging of acoustic wave fields;[15] since on corrugated surfaces it is sensitive to both the vertical and lateral displacement components, the SAW–STM is also suited—as we will show here—to measure the ratio u_1/u_3 of the oscillation ellipse of a SAW.

The article is organized as follows: In Sec. II we give a short introduction to the operation of a SAW–STM and details of the actual experiments. Section III provides the theoretical framework for evaluating the results obtained with an SAW–STM; in particular, we present a theory for the constant–current scanning mode. In Secs. IV and V we apply the theory to investigate the atomic movement involved in a Rayleigh wave on $LiNbO_3$ and to determine quantitatively amplitude and eccentricity of the oscillation ellipse. The article is concluded by the summarizing discussion of Sec. VI.

II. SAW–STM OPERATION AND EXPERIMENTAL DETAILS

The experimental setup of an SAW–STM is schematically illustrated in Fig. 1. The sample is a piezoelectric single crystal carrying an interdigital transducer (IDT) for exciting the SAW as well as a thin conducting layer for the tunneling experiment. The SAW-induced surface oscillation at the frequency $f_{\mathrm{SAW}}=\omega_{\mathrm{SAW}}/2\pi$ gives rise to a high frequency (HF) contribution in the tunneling current between tip and conducting layer. It is mixed at the nonlinear current–distance characteristics of the tunneling gap with a HF voltage V_{mod} at the frequency $f_{\mathrm{SAW}}+\Delta f$, which is added to the common dc tunneling voltage V_0. The mixing signal at the difference frequency Δf is chosen to be in the kHz range, where it can be easily analyzed by conventional STM electronics and lock-in technique. The mixing signal exhibits the amplitude and phase information of the SAW and—as we will show in the following sections—can be used to quantitatively determine the eccentricity of the SAW oscillation ellipse.

The experiments presented here were performed in an ultrahigh vacuum (UHV) system consisting of separate chambers for sample preparation and SAW–STM investigation. The UHV SAW–STM—developed recently in our group–[16] is based on a commercial Omicron STM-1 and has been modified by adding a UHV-compatible high-frequency wiring system for SAW excitation and signal detection. The sample is $YZ-$cut $LiNbO_3$ carrying a lithographically fabricated IDT with a resonance frequency of 40 MHz. It is mounted onto the sample holder which allows for flexible sample transfer into and within the UHV system. When the sample holder is inserted into the SAW–STM all required electrical connections to the sample are routinely established by contact springs. For the SAW–STM experiments a continuous gold film was used as a conducting layer; it was deposited *in situ* by electron beam evaporation; the deposition temperature was 300 K, the deposition rate 0.1 nm/s.

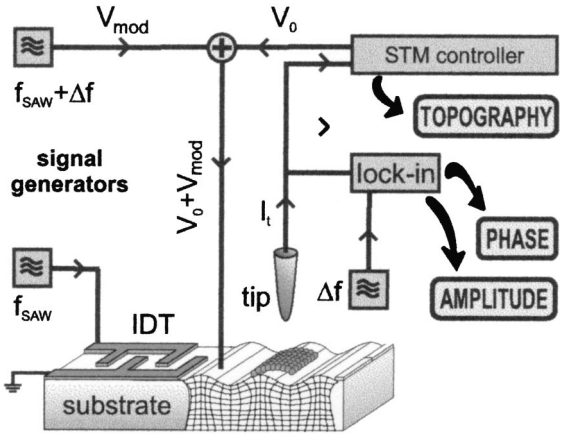

FIG. 1. Experimental setup of the SAW–STM for the measurement of SAW motion. The SAW-induced tunneling current modulation at the frequency f_{SAW} is mixed with the modulation of the tunneling voltage $(f_{\mathrm{SAW}}+\Delta f)$ at the nonlinear current–distance characteristic of the tunneling gap. A lock-in amplifier extracts the resulting difference frequency signal (Δf) yielding amplitude and phase of the SAW, which both are recorded in addition to the topography.

III. THEORY OF SAW–STM

In this section we provide the theoretical basis for evaluation of the amplitude and phase images recorded with an SAW–STM in the constant–current scanning mode. Our starting point is a model for the constant-height scanning mode described in Refs. 11 and 12 and we discuss the dependence of amplitude and phase of the mixing signal on topography in Sec. III A. In Sec. III B we extend the model to the more common constant–current scanning mode. Finally we compare both scanning modes by means of numerical simulations.

A. SAW-STM in the constant-height mode

The following derivation is performed for Rayleigh-type waves; however, the SAW–STM can be applied to all types of SAWs. To simplify, we treat the tunneling gap geometry in the reference frame of the sample surface, i.e., the sample being at rest and the STM tip traveling along a path defined by the oscillation ellipse (see Fig. 2). For MHz range SAW frequencies, the acoustic wavelength is large compared with typical dimensions of STM images, therefore the term $k_{\mathrm{SAW}}x_1$ in Eqs. (1) and (2) can be neglected. For modeling the tunneling gap it is assumed that all electrons tunnel along the shortest line between the apex of the tip and the sample surface. As typical SAW amplitudes are smaller $(<1\ \text{Å})$ than interatomic distances, the actual surface corrugation can be approximated by the tangential plane T through point $P_{s,0}$ which is closest to the center $P_{\mathrm{tip},0}$ of the tip oscillation ellipse. The resulting tunneling distance $d(t)$ then is the sum of the average distance d_0 and the harmonic frequency component due to the surface oscillation

$$d(t)=d_0+d_1\cos(\omega_{\mathrm{SAW}}t-\varphi); \tag{3}$$

where d_1 and φ are the amplitude and the phase of the distance modulation, which we briefly call distance amplitude and distance phase, respectively. Figure 1 shows the projection of the oscillation ellipse onto the surface normal

$\overline{P_{s,0}, P_{\mathrm{tip},0}}$ being $2d_1$. We now introduce the ellipse angle $\beta = \arctan(u_1/u_3)$, $u_0 = \sqrt{u_1^2 + u_3^2}$, $g_x = (\tan\gamma_x)^2$, and $g_y = (\tan\gamma_y)^2$, where γ_x and γ_y are the inclination angles of the tangential plane T in the directions parallel and perpendicular to the SAW propagation direction, respectively. According to the model in Refs. 11 and 12, d_1 and φ can be expressed as

$$d_1 = u_0 \sqrt{\frac{\sin^2\beta}{1 + \frac{g_y}{g_x} + \frac{1}{g_x}} + \frac{\cos^2\beta}{1 + g_x + g_y}}, \tag{4}$$

$$\varphi = \arctan(\tan\beta \tan\gamma_x) - \frac{\pi}{2}. \tag{5}$$

As discussed in Sec. II, the SAW-induced high frequency modulation of the tunneling current must be down-converted to the kHz band for detection by the STM electronics. For that purpose, a modulation voltage $V_{\mathrm{mod}} = V_1 \cos[(\omega_{\mathrm{SAW}} + \Delta\omega)t]$ at a frequency shifted from f_{SAW} by $\Delta f = 2\pi\Delta\omega$ is added to the tunneling voltage V_0

$$V(t) = V_0 + V_1 \cos[(\omega_{\mathrm{SAW}} + \Delta\omega)t]. \tag{6}$$

The tunneling current $I(t)$ is calculated via Simmons' formula[17]

$$I(d, V) = \frac{e^2\kappa}{2\pi h} \frac{V}{d} e^{-2\kappa d} \tag{7}$$

by using the series expansions $1/(1+x) = \Sigma_{n=0}^{\infty}(-1)^n(1-x)$ and $e^x = \Sigma_{n=0}^{\infty} x^n/n!$ as well as $\cos(x) = (e^{ix} + e^{-ix})/2$ (see Refs. 18 and 19). κ and h are the reciprocal decay length of the tunneling current and Planck's constant, respectively. $I(t)$ contains a series of Fourier components of which only the dc part I_{DC} and the difference frequency signal $I_{\Delta\omega}$ are of interest. With $I_0(d_0, V_0)$ denoting the undisturbed tunneling current at $V_1 = 0$ and $d_1 = 0$ we obtain by Eq. (7)

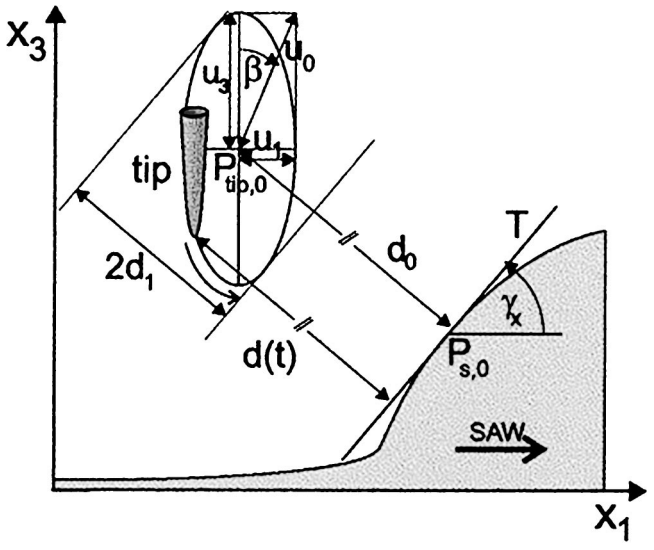

FIG. 2. SAW–STM experiment with Rayleigh-type waves: In the reference frame of the resting sample surface the SAW is described by an oscillatory motion of the STM tip on the path of the oscillation ellipse. The tunneling path of length $d(t)$ is approximated by the shortest distance between the tip and the tangential plane through the surface point $P_{s,0}$.

$$I_{\mathrm{DC}}(d_0, d_1, V_0) = H(d_0, d_1, 0)\, I_0(d_0, V_0), \tag{8}$$

$$I_{\Delta\omega}(d_0, d_1, V_0, V_1) = H(d_0, d_1, 1)\, I_0(d_0, V_0) \times \cos(\Delta\omega t - \varphi), \tag{9}$$

where the coefficients $H(d_0, d_1, 0)$ and $H(d_0, d_1, 1)$ are defined as

$$H(d_0, d_1, 0) = \sum_{m=0}^{\infty} \left[\binom{2m}{m} \frac{1}{2^{2m}} \sum_{\nu=0}^{2m} \frac{(2\kappa d_0)^\nu}{\nu!} \right] \left(\frac{d_1}{d_0}\right)^{2m}, \tag{10}$$

$$H(d_0, d_1, 1) = \frac{V_1}{V_0} \sum_{m=0}^{\infty} \left[\frac{\binom{2m+1}{m}}{2^{2m+1}} \sum_{\nu=0}^{2m+1} \frac{(2\kappa d_0)^\nu}{\nu!} \right] \times \left(\frac{d_1}{d_0}\right)^{2m+1}. \tag{11}$$

It is noteworthy that the phase of the difference frequency signal $I_{\Delta\omega}$ is equal to the distance phase φ. The term

$$A(d_0, d_1, V_0, V_1) \equiv H(d_0, d_1, 1)\, I_0(d_0, V_0) \tag{12}$$

is interpreted as the amplitude of the difference frequency signal obtained by the SAW–STM and denoted briefly as amplitude A. By defining a phase $\Phi \equiv \varphi + \pi/2$ the relation between the phase and the surface inclination can be expressed in the most simple way as $\Phi = \arctan\beta\tan\gamma_x$ [Eq. (5)]. While scanning the topography with an SAW–STM experiment, A and φ are simultaneously extracted from the tunneling current $I(t)$ by a lock-in amplifier tuned to Δf (see Fig. 1), which both may be displayed as greyscale images along with the topography image as in Fig. 7.

At the end of this section we want to address a specific flaw of the constant-height (index ch) operation mode in SAW–STM investigations. Since the average tunneling distance $d_0 = d_{0\mathrm{ch}}$ is kept constant, the surface approaches the STM tip due to the SAW oscillation, the larger the SAW amplitude; it may even collide with the tip when the distance amplitude d_1 exceeds $d_{0\mathrm{ch}}$. Figure 3(b) illustrates the influence d_1 on the amplitude of the mixing signal. We calculated A versus d_1 for different values of $d_{0\mathrm{ch}}$ by Eqs. (11) and (12) with $V_0 = V_1 = 1$ V. The plots of Fig. 3(b) demonstrate that A increases with d_1 and becomes infinite when the tip touches the surface for $d_1 = d_{0\mathrm{ch}}$.

Figure 3(a) summarizes the results of a series of SAW–STM experiments, where the amplitude A of the mixing signal was measured while varying the amplitude U_{IDT} of the high frequency voltage fed to the IDT. Note that the SAW displacement amplitudes u_1 and u_3 are proportional to U_{IDT}. The measurements were performed at a fixed sample position with $V_1 = 200$ mV, $V_0 = 80$ mV, and different values I_{DC}. The SAW–STM was operated in the constant–current mode, where the vertical tip position is controlled by electronic feedback to keep the average tunneling current constant. Obviously the experimental data in the constant–current mode—plotted as A versus U_{IDT} in Fig. 3(a)—clearly differ from the functional dependence A versus d_1 predicted for the constant–height mode [Fig. 3(b)]. Hence,

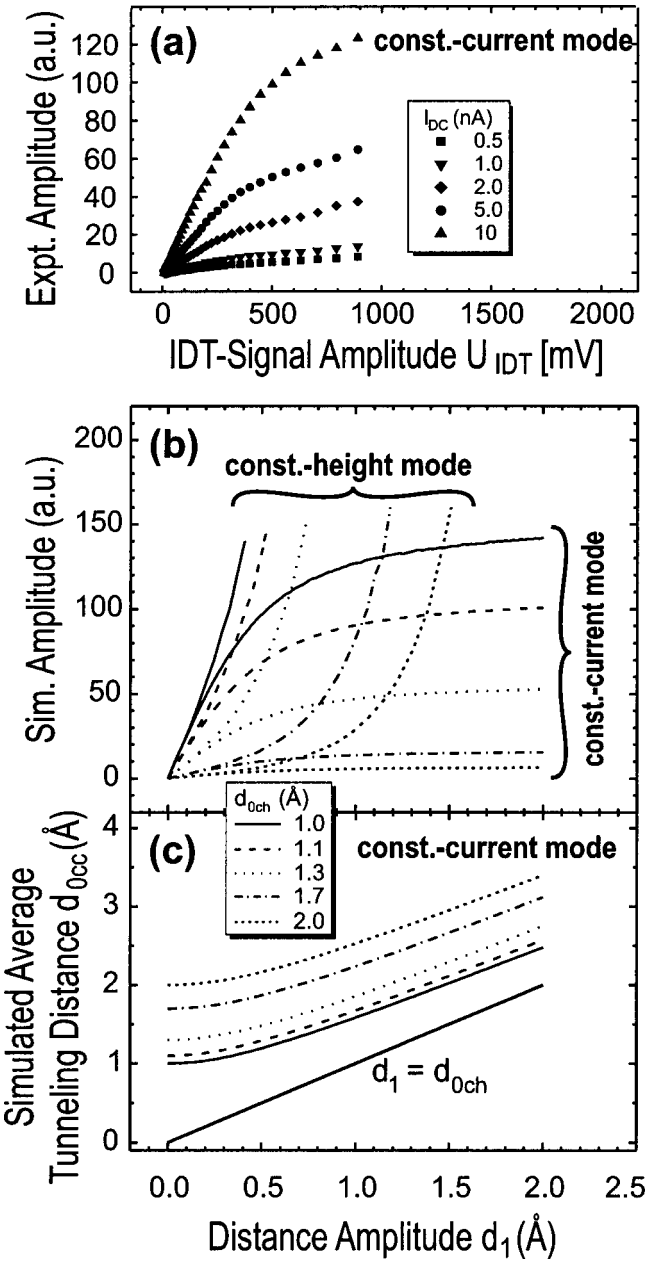

FIG. 3. SAW–STM operation in the constant–current and constant–height modes: (a) experimental amplitude A of the mixing signal as a function of the HF voltage U_{IDT} fed to the interdigital transducer to generate the SAW. (b) Influence of the amplitude d_1 of the tunneling distance modulation on A for the constant–height and the constant–current scanning modes. (c) Tunneling distance $d_{0\mathrm{cc}}$ as a function of d_1 calculated for different values of $d_{0\mathrm{ch}}$; due to the influence of d_1 on the average tunneling current I_{DC} the tip is retracted with increasing d_1, when operating in the constant–current mode.

the SAW–STM theory discussed so far needs further development to describe SAW–STM experiments in the constant–current mode properly.

B. SAW–STM in the constant–current mode

As discussed above the SAW–STM—as STMs, in general—is usually operated in the constant–current mode. According to Eq. (8) an increase of the distance amplitude d_1 causes a raise of the dc component I_{DC} of the tunneling current. As a consequence, the distance control of the STM electronics retracts the tip to keep I_{DC} at the preset value. For a theoretical description of this different operation mode, let us assume that initially the STM is operated in the constant–height mode without applying SAW. The tunneling current is obtained from Eq. (7) as

$$I_0(d_{0\mathrm{ch}}, V_0) = \frac{e^2\kappa}{2\pi h}\frac{V_0}{d_{0\mathrm{ch}}}e^{-2\kappa d_{0ch}}, \tag{13}$$

where $d_{0\mathrm{ch}}$ is the tunneling distance. Still operating the SAW–STM in the constant-height mode, the SAW is switched on, causing the dc component of the tunneling current to increase according to Eq. (8)

$$I_{\mathrm{DC}}(d_{0\mathrm{ch}}, d_1) = H(d_{0\mathrm{ch}}, d_1, 0)\, I_0(d_{0\mathrm{ch}}, V_0). \tag{14}$$

When eventually the constant-current (index cc) mode is activated the distance control retracts the tip to keep the dc component I_{DC} of the tunneling current equal to $I_0(d_{0\mathrm{ch}}, V_0)$. With $d_{0\mathrm{cc}}$ denoting the new average tunneling distance, we obtain by Eq. (9)

$$\begin{aligned} I_0(d_{0\mathrm{ch}}, V_0) &= I_{\mathrm{DC}}(d_{0\mathrm{cc}}, d_1, V_0) \\ &= H(d_{0\mathrm{cc}}, d_1, 0)\, I_0(d_{0\mathrm{cc}}, V_0), \end{aligned} \tag{15}$$

where $I_0(d_{0\mathrm{cc}}, V_0)$ is calculated with Eq. (7).

As Eq. (15) cannot be transformed to an analytical form, we solved it numerically for $d_{0\mathrm{cc}}$. This yields the average tunneling distance

$$d_{0\mathrm{cc}} = d_{0\mathrm{cc}}(d_{0\mathrm{ch}}, d_1) \tag{16}$$

as a function of the tunneling distance $d_{0\mathrm{ch}}$ of the undisturbed surface and of the distance amplitude d_1. Note that $d_{0\mathrm{cc}}(d_{0\mathrm{ch}}, d_1)$ is independent of V_0, as follows from Eqs. (7) and (15). In Fig. 3(c) $d_{0\mathrm{cc}}(d_{0\mathrm{ch}}, d_1)\big|_{d_{0\mathrm{ch}}=\mathrm{const}}$ is plotted for several values of $d_{0\mathrm{ch}}$, using Eq. (16). For $d_1 = 0$, i.e., without SAW, $d_{0\mathrm{cc}} = d_{0\mathrm{ch}}$. With increasing d_1, the distance control retracts the tip. The minimal tip–sample distance $d_{0\mathrm{cc}} - d_1$ occuring during one oscillation cycle is always positive, i.e., the tip is prevented from crashing into the sample. It can be proven that $\lim_{d_1\to\infty}(d_{0\mathrm{cc}} - d_1) = 0$, indicating that the minimal tip–sample distance defined above approaches zero for high distance amplitudes d_1. This is confirmed by the fact that the dc tunneling current as observed with an oscilloscope becomes unstable at high SAW amplitudes.

To calculate amplitude A in the constant-current mode, we insert $d_0 = d_{0\mathrm{cc}}$ given by Eq. (16) into Eq. (12)

$$\begin{aligned} &A(d_{0\mathrm{cc}}(d_{0\mathrm{ch}}, d_1), d_1, V_1) \\ &\quad = \frac{V_1}{V_0} H(d_{0cc}(d_{0ch}, d_1), d_1, 1)\, I_0(d_{0\mathrm{cc}}(d_{0\mathrm{ch}}, d_1), V_0). \end{aligned} \tag{17}$$

Keeping in mind that $I_{\mathrm{DC}} = I_0(d_{0\mathrm{ch}}, d_1)$ is the constant average tunneling current, we now solve Eq. (13) for $d_{0\mathrm{ch}}$ in order to insert $d_{0\mathrm{ch}}(I_0, V_0)$ into Eq. (17). This yields the rather complex term $A(d_{0\mathrm{cc}}(d_{0\mathrm{ch}}(I_0, V_0), d_1), d_1, V_1)$. The amplitude depends solely on the experimental input parameters V_0, V_1, d_1, and I_0. For a more explicit description, we

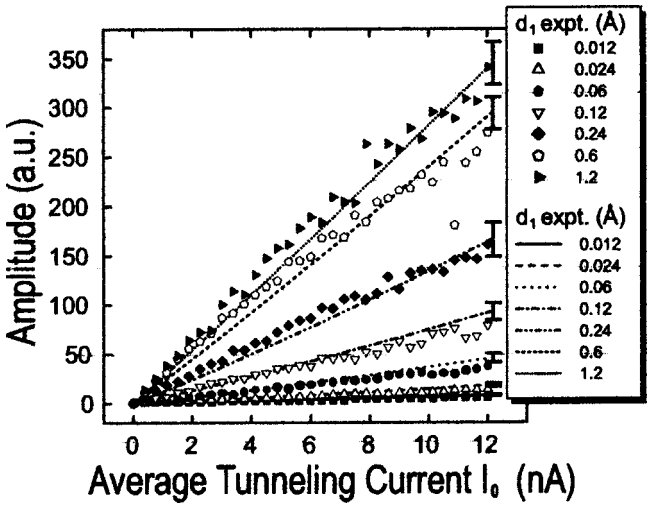

FIG. 4. Experimental and calculated dependence of the amplitude A of the mixing signal on the average tunneling current I_0, which is kept constant in the constant–current mode.

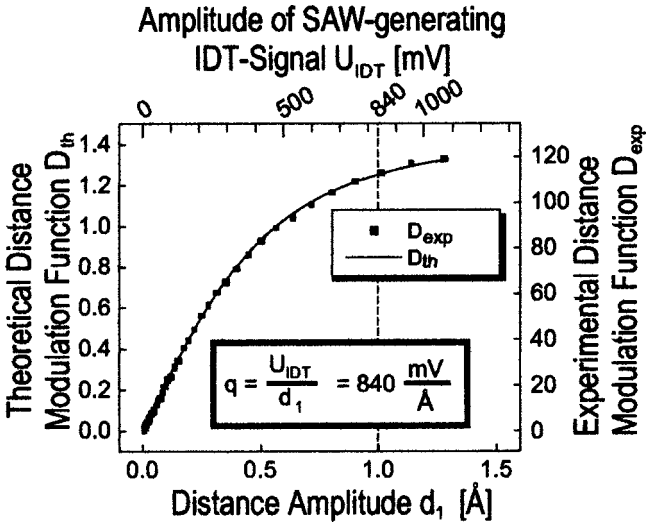

FIG. 5. Quantitative determination of the transverse displacement amplitude u_3 of the SAW by comparing the experimental and the theoretical distance modulation functions D_{exp} and D_{th}, respectively. Adjustment of the x scales of both curves yields the proportionality factor q between the amplitude U_{IDT} of the IDT voltage and the distance amplitude d_1.

numerically analyzed the functional dependence of A on these parameters finding that for $d_{0\mathrm{ch}}>2$ Å the amplitude can be approximated by

$$\tilde{A}(I_0, d_1, V_0, V_1)=\frac{V_1}{V_0^{1.05}}L(I_0)\,D(d_1). \tag{18}$$

The tilda indicates the change of explicit parameters compared to A as defined in Eq. (12). For an experimental confirmation of Eq. (18) we measured the amplitude A upon varying each of the parameters V_0, V_1, d_1, and I_0, while keeping the other three parameters constant. A slight deviation from the V_1 proportionality of A was found, indicating that the tunneling resistance is not purely ohmic as described by Eq. (7). Possibly due to this nonohmic behavior, the measured V_0 dependance of A is described best by $V_0^{-0.8}$ in contrast to $V_0^{-1.05}$ according to Eq. (18). The I_0 dependence of A is described by the tunneling current function $L(I_0)$, which for $I_0<20$ nA is a straight line through the origin. As can be seen from Fig. 4 the measured plot $\tilde{A}(I_0, d_1, V_0, V_1)\,|_{d_1,V_0,V_1=\mathrm{const}}$ is in good agreement with the I_0 dependence predicted by Eq. (18). The relation between d_1 and the experimental parameter U_{IDT} which is required for this comparison will be derived in Sec. IV.

In Fig. 3(b) the constant-current mode d_1 dependence $A(d_{0\mathrm{cc}}(d_{0\mathrm{ch}}, d_1), d_1, V_1)\,|_{d_{0\mathrm{ch}}=\mathrm{const},V_1=1V}$ given by Eq. (17) is plotted for different values of $d_{0\mathrm{ch}}$. In contrast to the constant–height curves also displayed in Fig. 3(b) the slope of the curves decreases with increasing d_1 because of the continuing retraction of the tip. Despite their obvious difference the constant–current and the constant–height curves in Fig. 3(b) have a common tangent at $d_1=0$. The plotted theoretical constant–current mode d_1 dependence of amplitude A is in good qualitative agreement with the experimentally obtained plots of $A(U_{\mathrm{IDT}})$ [compare Fig. 3(a)].

IV. MEASUREMENT OF SAW AMPLITUDE

A main objective of this work is the quantitative characterization of the surface oscillation in a Rayleigh-type wave, which requires the measurement of the transverse (u_3) and longitudinal (u_1) displacement amplitudes of the oscillation ellipse in absolute numbers. In this section, we focus on the calibrated measurement of the distance amplitude d_1, yielding u_3 of the SAW. The key for the determination of d_1 is the distance modulation function $D(d_1)$, which describes the d_1 dependence of the amplitude [Eq. (18)]. From the curves $A(d_{0\mathrm{cc}}(d_{0\mathrm{ch}}, d_1), d_1, V_1)\,|_{d_{0\mathrm{ch}}=\mathrm{const},V_1=1V}$ and from the curves $A(U_{\mathrm{IDT}})$ the theoretical and the experimental distance modulation functions $D_{\mathrm{th}}(d_1)$ and $D_{\mathrm{exp}}(U_{\mathrm{IDT}})$ can be extracted. To determine d_1 in absolute values it is sufficient to find the proportionality factor $q=U_{\mathrm{IDT}}/d_1$, which relates d_1 with the amplitude of the IDT-voltage U_{IDT} generating the SAW. For that purpose, we plotted both $D_{\mathrm{th}}(d_1)$ and $D_{\mathrm{exp}}(U_{\mathrm{IDT}})$ in the same diagram with separate x and y scales for the two data sets (Fig. 5). The latter were adjusted in a way to match $D_{\mathrm{th}}(d_1)$ with $D_{\mathrm{exp}}(U_{\mathrm{IDT}})$. Comparison of the d_1 scale of $D_{\mathrm{th}}(d_1)$ with the U_{IDT} scale of $D_{\mathrm{exp}}(U_{\mathrm{IDT}})$ yields the proportionality factor $q=(840\pm 90)$ mV/Å. The error was obtained from analyzing the data of $D_{\mathrm{exp}}(U_{\mathrm{IDT}})$ measurements at several values of V_0 and V_1. Assuming that the data $D_{\mathrm{exp}}(U_{\mathrm{IDT}})$ were collected at horizontal sample positions ($\gamma_x=\gamma_y=0$) Eq. (4) yields $d_1=u_3$. Hence, q is the proportionality factor between u_3 and the amplitude U_{IDT} of the SAW-generating signal fed to the IDT. From this calibration, the transverse displacement amplitude u_3 can be calculated from the respective U_{IDT} chosen in the experiment.

To figure out the dynamic range of our UHV–SAW–STM we measured the amplitude A as a function of the SAW frequency for values $U_{\mathrm{IDT}}=1$, 10, 100, and 1000 mV (Fig. 6). These curves were compared to the frequency dependence of the transmission S_{12} determined with the help of a

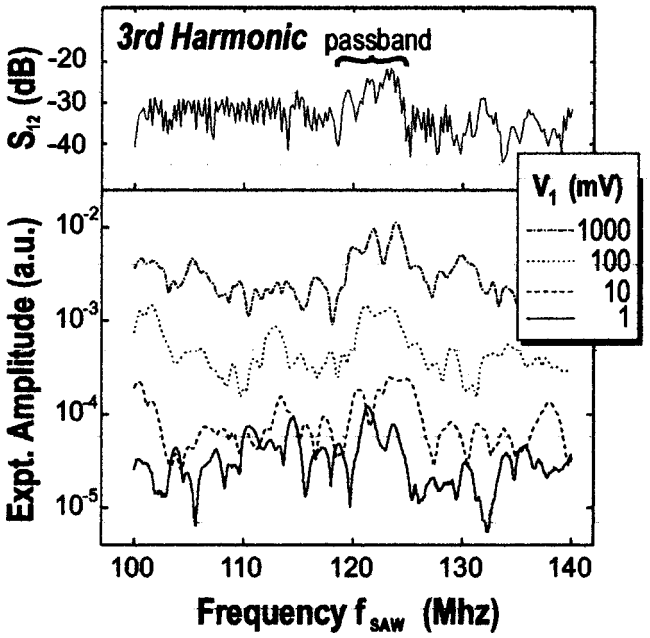

FIG. 6. Frequency dependence of the transmission S_{12} and of the amplitude of the mixing signal measured by the SAW–STM at the third harmonic frequency of the IDT. Notice that for all values of U_{IDT} the amplitude reproduces the IDT passband revealing a sensitivity of the UHV SAW–STM for amplitudes as small as 0.001 Å.

second ''receiver'' IDT on the $LiNbO_3$ sample, which receives the SAW of the ''sender'' IDT and converts it back to an electrical signal. The transmission S_{12} is defined as the ratio of the amplitude of the received signal to the amplitude of the SAW-generating signal. The plot of S_{12} in Fig. 6 reveals a passband around 120 MHz corresponding to the third harmonic of the IDT. Also the amplitude plots of Fig. 6 show a maximum at the position of the transmission passband, thus verifying that in the frequency interval of this passband the difference frequency signal is caused by the SAW rather than by any parasitic contribution. The plot $A(f_{SAW})$ for $U_{IDT}=1$ mV still displays that maximum, suggesting that the UHV–SAW–STM indeed is capable of detecting SAWs with a transverse displacement amplitude $u_3=0.0012$ Å. Obviously the dynamic range of our UHV–SAW–STM comprises at least 3 orders of magnitude down to SAW amplitudes as small as 0.001 Å.

V. MEASUREMENT OF OSCILLATION ELLIPSE ECCENTRICITY

For a quantitative determination of the oscillation ellipse geometry it is sufficient to know the transverse displacement amplitude u_3 and the ellipse angle β which describes the eccentricity of the oscillation ellipse. Thus, after having determined u_3 we now present a routine to extract β from the experimental phase images.

Figure 7(a) shows the topography of the gold film, which is characterized by a grainy morphology; the dotted line indicates the propagation direction of the SAW. According to Eqs. (4) and (5) amplitude and phase of the distance modulation and hence also amplitude A and phase Φ of the difference frequency are affected by β and the local surface incli-

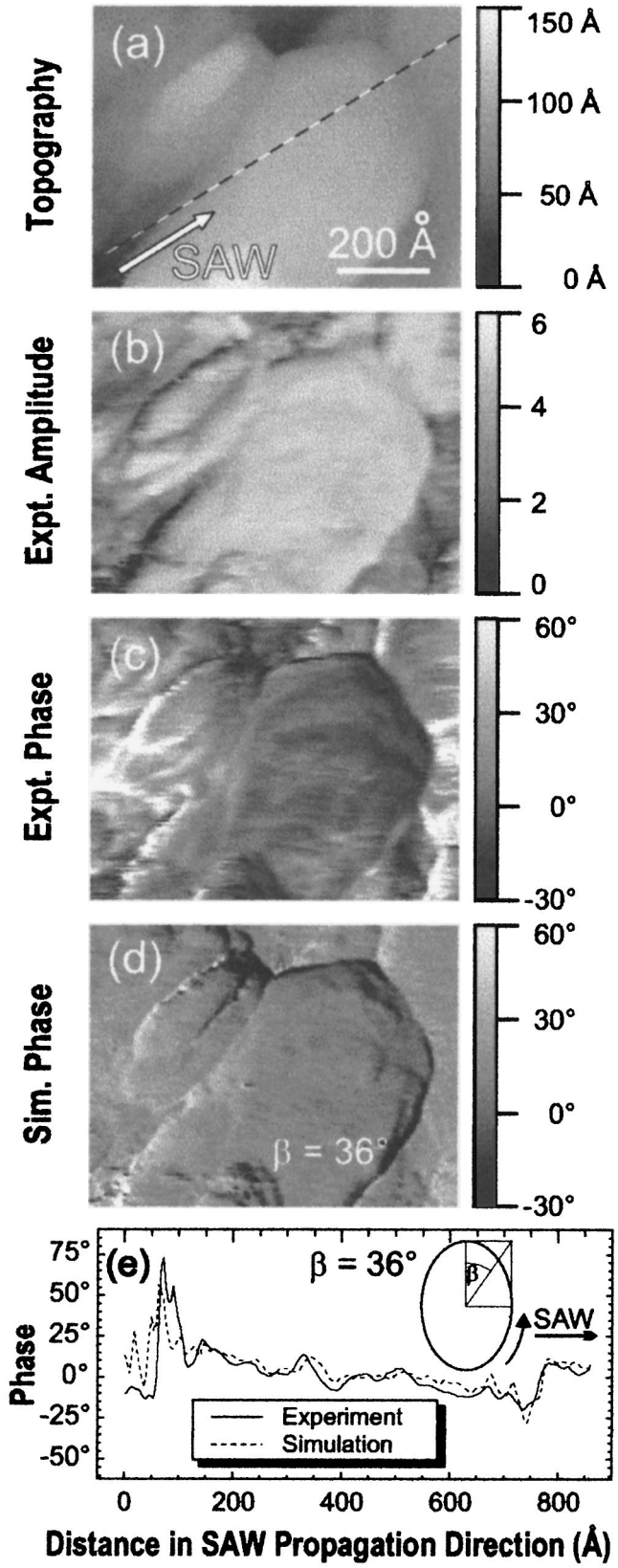

FIG. 7. (a) Topography of a gold film on $LiNbO_3$ as well as (b) amplitude and (c) phase of a Rayleigh wave, all recorded simultaneously with the SAW–STM. (d) Simulated phase image with an ellipse angle $\beta=36°$ yielding good agreement with experiment (c). (e) Profiles of the experimental and simulated phase along the dotted line in (a).

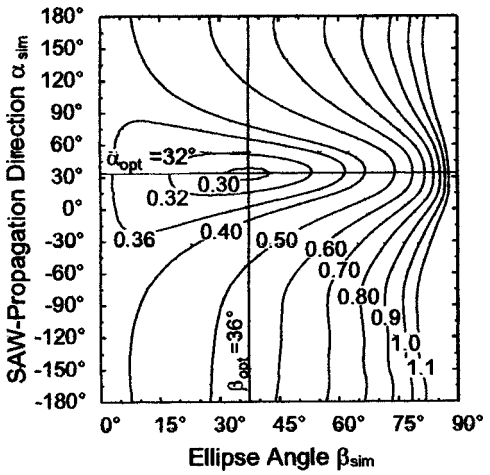

FIG. 8. Correlation error field corresponding to the phase measurement displayed in Fig. 7. The correlation error is used to quantify the difference between the experimental and simulated phase images, with the ellipse angle β_{sim} and the propagation direction α_{sim} being the input parameters for the simulation. At the minimum of the correlation error field ($\beta_{opt}=36°$, $\alpha_{opt}=32°$) the agreement between the experimental and simulated phase images is best.

nation given by γ_x and γ_y. Therefore also in the experimental amplitude and phase images - displayed in Fig. 7 (b) and (c), respectively, the morphology of the corrugated gold film can be recognized. Because of the derivatives occurring in Eqs. (4) and (5), the structural features are even more pronounced in amplitude and phase images compared with topography. Figure 7(d) shows a phase image simulated by Eq. (5) using the experimental topography of Fig. 7(a) and $\beta=36°$ as input parameters. The simulated phase image is in good agreement with the experimental phase image of Fig. 7(c); it reproduces the main structural features on a quantitative level, as is further corroborated by the nearly identical experimental and simulated phase profiles along the dotted line indicated in Fig. 7(a).

In order to determine the optimum value of β, yielding the best agreement with experiment, we simulated phase images with different ellipse angles β_{sim} and different wave propagation directions α_{sim} as input parameters (α_{opt} is defined as the angle between the propagation direction and the fast scanning direction). The simulated phase images $\Phi_{\beta_{sim},\alpha_{sim}}$ then are compared with the experimental phase image Φ_{exp}. The values β_{sim} and α_{sim}, for which optimum agreement with experiment is obtained, are interpreted as β_{opt} and α_{opt}. For an impartial judgement of this agreement, we introduce the correlation error R_Φ between two phase images. With (i,j) being the pixel coordinates, R_Φ is defined to be proportional to the standard deviation σ of the values $\Phi_{\beta_{sim},\alpha_{sim}}(i,j)-\Phi_{exp}(i,j)$. In order to shift the obtained phase values into the interval $[0°, 180°]$ we introduce a function $D:[-360°, +360°]\rightarrow[0°, 180°]$ and define the correlation error as

$$R_\Phi(\beta_{sim}, \alpha_{sim}) =^{def} \frac{\sqrt{12}}{180°}\sigma(D(\Phi_{exp}-\Phi_{\beta_{sim},\alpha_{sim}})). \quad (19)$$

The normalizing factor $\sqrt{12}/180°$ guarantees that the error correlation of two pictures with randomly distributed pixel values is equal to 1.

By plotting $R_\Phi(\beta_{sim}, \alpha_{sim})$ as a function of the ellipse angle β_{sim} and of the propagation direction α_{sim} the error correlation field of Fig. 8 is obtained. $R_\Phi(\beta_{sim}, \alpha_{sim})$ exhibits a clear minimum at $\beta_{sim}=36°$ and $\alpha_{sim}=32°$, indicating that for these parameters the agreement between the simulated and experimental phase images is best. Therefore we interpret $\beta_{sim}=36°$ as the optimum ellipse angle β_{opt} to represent the experiment. β_{opt} is close to the value $\beta=35.1°$ which is calculated from the elastic constants of $LiNbO_3$ by Slobodnik *et al.*[20] After measuring both the transverse displacement amplitude and the ellipse angle, the complete geometry of the oscillation ellipse is determined.

The correlation error field displayed in Fig. 8 was calculated on basis of the entire scanned area of the images of Fig. 7. We found that reasonable correlation error fields can be obtained by restricting the comparison between the simulated and the measured images on a part of the scanned area. The smallest partial scanned area yielding an error correlation field with a well defined minimum has dimensions of 30×30 Å. These promising results therefore demonstrate that the SAW–STM method presented here is suited to measure elastic constants on a nanometer scale.

VI. CONCLUSIONS

We have investigated the surface oscillation due to a Rayleigh wave on $LiNbO_3$ using our UHV–SAW–STM. Here the high frequency signal due to the SAW is extracted from the tunneling current by mixing with a slightly detuned HF voltage added to the dc tunneling voltage; the mixing signal at the difference frequency reflects amplitude and phase of the SAW. To evaluate our experimental data we had to extend the current theory for SAW–STM, which is valid only for the constant-height scanning mode, to the more common constant–current scanning mode. In order to verify our theory we investigated the dependence of the mixing signal on various experimental parameters and achieved good agreement with experiment. Only for the V_0 and the V_1 dependences were small deviations found, which can be explained by a tunneling characteristic that is not purely ohmic.

Supplied with a proper theoretical basis the UHV–SAW–STM proves to be a powerful technique for quantitative investigations of the atomic movement induced by the Rayleigh waves. By comparing the experimental and theoretical dependence of the mixing signal amplitude on the amplitude of the tunneling distance modulation, we succeded in determining the transverse displacement amplitude u_3 of the SAW in absolute numbers. From the distance calibration it can be concluded that our UHV–SAW–STM is capable of generating and detecting surface acoustic waves with transverse displacement amplitudes as small as 0.001 Å. Furthermore, via comparison of experimental and simulated SAW–STM phase images we also succeeded in quantitatively determining the eccentricity of the Rayleigh wave oscillation ellipse. The excellent agreement of the measured eccentricity with theoretical values further corroborates the validity of

the theoretical description. Moreover, our measurements revealed that the oscillation ellipse eccentricity can be determined with the high lateral resolution of a few nanometers. As local variations of the elastic properties influence the shape of the oscillation ellipse, imaging of elastic inhomogeneities may become accessible with the SAW–STM in future experiments. Finally we note that SAW–STM is not restricted to investigations of Rayleigh waves as presented here. Only minor modifications of the theory describing the inclination dependence of the SAW–STM signal are necessary to apply the method of SAW–STM to quantitative investigations of SAW modes other than Rayleigh waves.

ACKNOWLEDGMENTS

The authors wish to thank S. Krauß for technical support, W. Seidel for providing the IDT samples, J. Yang for assisting in calibration, and E. Chilla and K.H. Ploog for helpful discussions. The work was sponsored by the European Union (EFRE).

[1] Lord Rayleigh, Proc. London Math. Soc. **17**, 4 (1885).
[2] A. E. H. Love, *Some Problems of Geophysics* (Cambridge University Press, London, 1911).
[3] T. Sogowa, P. Santos, S. K. Zhang, S. Eshlagi, A. D. Wieck, and K. H. Ploog, Phys. Rev. Lett. **87**, 276601 (2001).
[4] P. V. Santos, M. Ramsteiner, and R. Hey, Phys. Status Solidi B **215**, 253 (1999).
[5] J. P. Monchalin, IEEE Trans. Ultrason. Ferroelectr. Freq. Control **33**, 485 (1986).
[6] G. C. Wetsel, Jr., S. E. McBridge, R. J. Warmack, and B. Van de Sande, Appl. Phys. Lett. **55**, 528 (1989).
[7] W. Rohrbeck and E. Chilla, Phys. Status Solidi **131**, 69 (1992).
[8] O. Kolosov and K. Yamanka, Jpn. J. Appl. Phys., Part 2 **32**, L1095 (1993).
[9] K. Yamanka, H. Ogiso, and O. Kolosov, Appl. Phys. Lett. **64**, 178 (1994).
[10] K. J. Strozewski, S. E. McBride, and G. C. Wetsel, Jr., Ultramicroscopy **42–44**, 388 (1992).
[11] E. Chilla, W. Rohrbeck, H.-J. Fröhlich, R. Koch, and K. H. Rieder, Appl. Phys. Lett. **61**, 3107 (1992).
[12] E. Chilla, W. Rohrbeck, H.-J. Fröhlich, R. Koch, and K. H. Rieder, Ann. Phys. (N.Y.) **3**, 21 (1994).
[13] J. Heil, J. Wesner, and W. Grill, J. Appl. Phys. **64**, 1939 (1988).
[14] W. Sauer, M. Streibl, T. H. Metzger, A. G. C. Haubrich, S. Manus, A. Wixforth, A. Mazuelas, J. Härtwig, and J. Baruchel, Appl. Phys. Lett. **75**, 1709 (1999).
[15] T. Hesjedal, E. Chilla, and H.-J. Fröhlich, Appl. Phys. Lett. **69**, 354 (1996).
[16] P. U. Voigt, S. Krauß, E. Chilla, and R. Koch, J. Vac. Sci. Technol. A **19**, 1817 (2001).
[17] J. G. Simmons, J. Appl. Phys. **34**, 1793 (1963).
[18] W. Rohrbeck, E. Chilla, H.-J. Fröhlich, and J. Riedel, Appl. Phys. A: Solids Surf. **52**, 344 (1991).
[19] E. Chilla, W. Rohrbeck, H.-J. Fröhlich, and J. Riedel, Acoust. Imaging **19**, 737 (1992).
[20] A. J. Slobodnik, E. D. Conway, and R. T. Delmonico, *Microwave Acoustic Handbook*, (NTIS, Springfield, VA, 1973).